Near Infrared-Activatable Biomimetic Nanogels Enabling Deep Tumor Drug Penetration Completely Inhibit Orthotopic Glioblastoma

Dongya Zhang
Henan-Macquarie University Joint Centre for Biomedical Innovation, School of Life Sciences, Henan University
Sidan Tian
Huazhong University of Science and Technology
Yanjie Liu
Henan University
Meng Zheng
Henan University
Yan Zou
Henan University
Bingyang Shi
Henan-Macquarie Uni Joint Centre for Biomedical Innovation, School of Life Sciences, Henan University
Liang Luo (liangluo@hust.edu.cn)
Huazhong University of Science and Technology https://orcid.org/0000-0001-9274-1866

Article

Keywords:

Posted Date: January 27th, 2022

DOI: https://doi.org/10.21203/rs.3.rs-1250591/v1

Version of Record: A version of this preprint was published at Nature Communications on November 11th, 2022. See the published version at https://doi.org/10.1038/s41467-022-34462-8.

Abstract

Glioblastoma multiforme (GBM) is one of the most fatal malignancies due to the existence of blood-brain barrier (BBB) and the difficulty to maintain an effective drug accumulation in deep GBM lesions. Here we present a novel biomimetic nanogel system that can be precisely activated by near infrared (NIR) irradiation to achieve facilitated BBB crossing and deep tumor penetration of drugs. Synthesized by crosslinking pullulan and poly(deca-4,6-diynedioic acid) (PDDA) and loaded with temozolomide and indocyanine green (ICG), the nanogels are inert to endogenous oxidative conditions but can be selectively disintegrated by ICG-generated reactive oxygen species upon NIR irradiation. Camouflaging the nanogels with apolipoprotein E (ApoE) peptide-decorated erythrocyte membrane further allows prolonged blood circulation and active tumor targeting to secure sufficient tumor accumulation. The precisely controlled NIR irradiation on tumor lesions excites ICG and concurrently activates the cumulated nanogels by deforming the nanogels and triggering burst drug release for facilitated BBB permeation and infiltration into distal tumor cells. These NIR-activatable biomimetic nanogels showed a great potency in orthotopic GBM-bearing mouse models that completely suppressed the tumor growth with significantly extended survival.

Background

Glioblastoma multiforme (GBM) is the most common primary tumor in the central nervous system, accounting for about 40% of the total intracranial malignant tumor incidence[1-2]. According to the World Health Organization classification, GBM is of grade IV histological malignancy and the median survival of glioblastoma patients is only about 12 months[3-4]. Although a variety of modalities, including surgery[5], radiotherapy[6], chemotherapy[7], and other emerging methods such as photodynamic therapy (PDT)[8], have been developed for GBM treatment, their performances are far below expectation with limited survival. In particular, to approach effective drug concentrations in the GBM lesions, which is highly desired for optimal therapeutic outcomes, suffers from extremely short blood circulation, limited blood-brain barrier (BBB) penetration, and insufficient tumor uptake[9-11]. Efficient delivery of intravenously administered therapeutics across the BBB and other biological barriers into the tumor remains an insurmountable challenge for GBM treatment.

Delivering therapeutics through engineered nanomaterials, or the so-called nanomedicines, has been considered revolutionary strategies in overcoming a series of biological barriers for anticancer treatment[12-13], and also offers an opportunity to integrate multiple treatment modalities[14-15]. However, to assert effective drug accumulation in GBM is still difficult, mostly because of inefficient drug extravasation and penetration in brain tumors, as well as the failure of tumor-specific drug release[16]. Although active ligands such as apolipoprotein E (ApoE) peptide can facilitate BBB crossing and tumor uptake of nanomedicines through specific ligand-receptor interactions[17-18], infiltration from blood vessels into GBM tumor tissue and to distal tumor cells remains largely inefficient for bulk nanoparticles. In addition, many nanocarriers responding to pH values, redox conditions, and tumor overexpressed

enzymes have been developed for tumor-specific drug release[19-23]. However, these stimulations based on tumor microenvironment (TME) are not readily applicable to nanomedicines in blood vessels. Even in the tumor regions, the TME that benefits the desired drug release is usually 100-200 μm away from the tumor blood vessel networks[22, 24-25]. Moreover, passive drug release based on TME stimulation can be misled by non-tumor conditions similar to TME[26-27]. For instance, reactive oxygen species (ROS)-responsive carriers represent a very promising category in nanomedicine, since most tumor tissues have shown higher ROS levels than normal[28-30]. However, inflammation or amyloid deposits in brain also induces high endogenous ROS levels[31-34], which can easily alter the designated drug release in GBM tumors and affect the therapeutic outcomes. Precisely activatable drug delivery nanoplatforms are therefore highly desired to warrant efficient BBB penetration and tumor-specific release of therapeutic agents for successful GBM treatment.

In this work, we have created a nanogel system by crosslinking pullulan and an oxidatively degradable conjugated polymer poly(deca-4,6-diynedioic acid), or PDDA[35]. PDDA is inert to endogenous oxidative conditions, but can completely degrade in the presence of ROS generated by photosensitizers upon light irradiation[36]. Loading both indocyanine green (ICG), an FDA-approved near infrared (NIR) photosensitizer, and temozolomide (TMZ), the first-line chemotherapeutic drug for GBM, into the nanogels yields NGs@TMZ/ICG, which are then camouflaged with ApoE peptide-decorated erythrocyte membranes for prolonged blood circulation and active tumor targeting. The enhanced stability of finally formed ARNGs@TMZ/ICG in physiological conditions allows them to cumulate efficiently in GBM lesions after intravenous administration. NIR light is then applied manually to activate ARNGs@TMZ/ICG when they reach maximal accumulation in GBM lesions. ICG can generate ROS to deform the nanogels and trigger the burst release of both TMZ and ICG for facilitated extravasation and deep tumor penetration. The accumulated TMZ and ICG in deep GBM lesions hence boost the efficacy of combined photodynamic-chemotherapy to completely alleviate orthotopic GBM tumors in mouse models, demonstrating that this NIR-activatable biomimetic nanogel system holds great potential as a clinical solution for brain tumor treatment.

Results

Synthesis and NIR-induced disintegration of NGs@TMZ/ICG. The NGs@TMZ/ICG are readily fabricated via two steps, the crosslinking between PDDA and pullulan and the co-loading of TMZ and ICG. As schematically illustrated in Fig. 2a**,** when 808 nm NIR irradiation is applied to NGs@TMZ/ICG, ICG generates ROS to completely degrade PDDA into succinic acid, a biocompatible small molecule that naturally occurs in organisms. The nanogels are therefore disintegrated to release TMZ and ICG accordingly. Dynamic light scattering (DLS) measurement showed that all prepared nanoparticles, including NGs@TMZ/ICG, single agent loaded nanogels NGs@TMZ and NGs@ICG, and blank nanogels containing no drug, showed similar hydrodynamic sizes of around 170 nm (Fig. 2b) and slightly negative surface charges (Fig. 2c). The transmission electron microscope (TEM) image of NGs@TMZ/ICG displayed their sphere morphologies with less than 200 nm in diameter. After NIR irradiation, the

nanoparticles exhibited apparent disintegration with decreased sizes and indistinct shapes (“NGs@TMZ/ICG + L” in Fig. 2d). The DLS measurement confirmed that the particle size of the nanogels decreased significantly after irradiation (Fig. 2e), further verifying the NIR-induced disintegration of NGs@TMZ/ICG.

To examine the degradation of PDDA, we loaded another classic photosensitizer Rose Bengal (RB) into the nanogels, and exposed them to 520 nm irradiation. With the increase of irradiation time, the color of the nanogels faded gradually, leaving only the color of RB (Fig. 2f). More interestingly, the fluorescence of RB in the nanogels was very weak at the beginning, due to the quench by PDDA through fluorescence resonance energy transfer. However, the fluorescence of RB boosted after the nanogels were exposed to the irradiation (bottom pictures, Fig. 2f), evidencing that the conjugated backbone of PDDA had been broken by the light irradiation (Supplementary Fig. 1). The chemical structural change of PDDA in NIR-induced disintegration of NGs@TMZ/ICG was further evaluated using Raman spectroscopy (Fig. 2g). The pristine NGs@TMZ/ICG exhibited two strong Raman peaks corresponding to the C=C bond (1522 cm^{-1}) and C≡C bond (2120 cm^{-1}) of PDDA backbone. Upon NIR irradiation, these two peaks decreased gradually yet synchronously (Fig. 2h), indicating the simultaneous cleavage of C=C and C≡C bonds in PDDA backbone during the decomposition. Collectively, we have successfully fabricated PDDA-based nanogels, and the ROS generated by photosensitizers upon NIR irradiation can decompose PDDA efficiently, hence allowing for the laser-controlled disintegration of the nanogels.

Preparation and NIR-induced deformation of ARNGs@TMZ/ICG. The prepared NGs@TMZ/ICG was then camouflaged with the ApoE peptide-decorated erythrocyte membranes (AR) by mechanical sonication to obtain the final biomimetic nanogels (ARNGs@TMZ/ICG). These biomimetic nanogels were deformable upon NIR irradiation (Fig. 3a). The AR-coated nanogels, including ARNGs@TMZ/ICG and the single drug loaded ARNGs@TMZ and ARNGs@ICG, had an average size of around 190 nm (Fig. 3b), slightly larger than the corresponding non-coated nanogels. In addition, their surface charges became more negative, evidencing the successful camouflaging by the membranes (Fig. 3c). We next examined whether NIR irradiation could induce the deformation of ARNGs@TMZ/ICG for the desired drug release. We studied the morphologies of ARNGs@TMZ/ICG before and after NIR irradiation using TEM imaging. The pristine nanogels were spherical with clearly visible erythrocyte membranes (Fig. 3d). However, after the 808 nm laser irradiation, although their erythrocyte membranes were preserved, the particles were deformed with irregular shapes (Fig. 3e). Interestingly, DLS measurement (Fig. 3f) demonstrated that the particle size of ARNGs@TMZ/ICG increased significantly after the irradiation. The Young’s moduli of ARNGs@TMZ/ICG, measured using atomic force microscopy (AFM), significantly reduced after the NIR irradiation, further evidencing the light-induced deformation of these nanogels (Fig. 3g). The nanogels wrapped inside the erythrocyte membranes were disintegrated upon NIR irradiation, making the ARNGs much softer and looser than before the irradiation. Accordingly, the in vitro release of TMZ and ICG from ARNGs@TMZ/ICG both increased significantly upon 808 nm laser irradiation (Fig. 3h, 3i), evidencing that the NIR irradiation promoted the drug release from the nanogels (Supplementary Fig. 2).

BBB penetration, tumor uptake, and cytotoxicity. To evaluate the BBB permeability of the biomimetic nanogels, we first set up an *in vitro* trans-well model by seeding a monolayer of endothelial cell bEnd.3 to mimic the BBB. TMZ was not included in this study to avoid possible toxicity to endothelial cells. The trans-endothelial electrical resistance (TEER) value of the monolayer bEnd.3 remained >200 Ω cm^2 throughout the study, confirming the integrity of the endothelial cell monolayer[37-38]. The cumulative transport ratio of ARNGs@ICG was significantly higher than that of RNGs@ICG, the nanogels coated by erythrocyte membranes but without ApoE peptide decoration (Fig. 4a). The enhanced BBB permeability through ApoE peptide functionalization was resulted from their high binding affinity with low density lipoprotein (LDL) receptors that were overexpressed in bEnd.3 cells[39-40]. Notably, NIR irradiation did not affect the transport of ARNGs across the mimic BBB layer (Supplementary Fig. 3).

We next assessed the cellular uptake of ARNGs@TMZ/ICG in U87MG human GBM cells. From confocal laser scanning microscope (CLSM) images, stronger red fluorescence was seen in cells treated with ARNGs@TMZ/ICG than those treated with RNGs@TMZ/ICG or mixed solution of TMZ and ICG ("Free TMZ/ICG"), indicating their efficient cellular uptake on basis of the receptor-mediated endocytosis (Fig. 4b). Intriguingly, the ICG fluorescence in cells treated with ARNGs@TMZ/ICG increased significantly after being exposed to 808 nm laser irradiation ("ARNGs@TMZ/ICG + L"). Since the fluorescence of ICG was quenched inside the nanogels, the boosted ICG fluorescence unambiguously evidenced that the NIR irradiation facilitated the release of ICG from the nanogels. Flow cytometry analysis further quantified the cellular uptake of various particles (Fig. 4c). Upon NIR irradiation, the ICG fluorescence of cell treated with ARNGs@TMZ/ICG was 1.5-fold higher than without NIR irradiation, and 2.8-fold higher than that of cells treated with RNGs@TMZ/ICG. We further evaluated the tumor uptake of ARNGs@TMZ/ICG using a 3D U87MG tumor spheroid model, and found that ICG fluorescence could be detected in the center of the tumor spheroids upon NIR irradiation. As a comparison, considerably weaker fluorescence was observed for the treatment without irradiation (Fig. 4d), indicating that NIR irradiation promoted the deep penetration of ICG to distal tumor cells.

The ability of ARNGs@TMZ/ICG to generate ROS upon 808 nm light irradiation was examined using U87MG cells stained with 2,7-dichlorodihydrofluorescein diacetate (DCFH-DA). As shown in Fig. 4e, when exposed to NIR irradiation, the cells treated with ARNGs@TMZ/ICG manifested stronger green fluorescence than those treated with RNGs@TMZ/ICG or free mixture of TMZ/ICG, indicating an efficient ROS production. The 3-(4,5-dimethylthiazol-2-yl)-2,5-diphenyltetrazolium bromide (MTT) assay showed that ARNGs@TMZ/ICG upon NIR irradiation (ARNGs@TMZ/ICG + L) resulted in more efficient tumor cell inhibition than the monotherapies (ARNGs@TMZ and ARNGs@ICG + L, Fig. 4f), evidencing that NIR had activated ARNGs@TMZ/ICG for a synergy of combined photodynamic and chemotherapy on GBM. The propidium iodide (PI) and Annexin V co-staining analysis further confirmed that ARNGs@TMZ/ICG + L triggered cell apoptosis efficiently (Fig. 4g). Collectively, NIR irradiation effectively activated ARNGs@TMZ/ICG through enhanced BBB penetration, tumor uptake, and cytotoxicity, which were essential for the subsequent in vivo alleviation of GBM.

Pharmacokinetics, in vivo BBB penetration, and biodistribution. The pharmacokinetics of intravenously injected nanogels was examined by measuring the plasma concentrations of TMZ and ICG in tumor-free mice. The elimination half-life of TMZ ($t_{1/2}$, α) was 7.6 h and 7.2 h for ARNGs@TMZ/ICG and RNGs@TMZ/ICG respectively, significantly longer than that of NGs@TMZ/ICG (2.3 h) (Fig. 5a). It should be noted that both ARNGs@TMZ/ICG and RNGs@TMZ/ICG maintained a high TMZ concentration for a period of up to 48 h, demonstrating that camouflaging with erythrocyte membrane could remarkably increase the circulation time of nanogels, which was important for sufficient drug accumulation in the tumor sites. The pharmacokinetic profile of ICG was similar to that of TMZ (Fig. 5b). As expected, the mixed solution of TMZ and ICG (Free TMZ/ICG) were rapidly excreted from the body with a short half-life of less than 5 min, consistent with previous reports[41-42].

We next evaluated the ability of different nanogels to traverse BBB in vivo, following a single tail vein injection in the orthotopic luciferase expressed U87MG (U87MG-Luc) tumor-bearing mouse model. 808 nm laser irradiation was applied on the tumor site at 4 h post injection, and the ICG fluorescence was monitored using an in vivo imaging system. As shown in Fig. 5c, the fluorescence of ICG quickly increased in brain within 2 h for mice treated with ARNGs@TMZ/ICG, either with or without NIR irradiation. The ICG fluorescence co-localized very well with the tumor bioluminescence, implying excellent targeting efficiency of ARNGs@TMZ/ICG. More strikingly, the ICG fluorescence increased remarkably upon NIR irradiation (ARNGs@TMZ/ICG + L) and maintained at a high level for up to 24 h, implying that the NIR irradiation triggered the burst drug release in tumor lesions. In contrast, both non-targeting RNGs@TMZ/ICG and uncoated NGs@TMZ/ICG displayed much weaker ICG fluorescence in brain, regardless NIR irradiation, suggesting their limited BBB penetration and tumor accumulation.

The biodistribution of TMZ and ICG delivered via various nanogels was examined by *ex vivo* images of the major organs taken from the mice receiving different treatments (Fig. 5d). The mouse treated with ARNGs@TMZ/ICG showed obviously stronger ICG fluorescence in brain than the mice treated with other nanogels, and NIR irradiation could induce even higher ICG fluorescence (ARNGs@TMZ/ICG + L). The exceptional BBB penetration as well as tumor accumulation of ARNGs@TMZ/ICG were mainly attributed to the receptor-mediated transcytosis, in that LDL receptor family was overexpressed by both endothelial cells of BBB (Supplementary Fig. 4) and U87MG brain tumor cells, which had a strong binding affinity with ApoE peptide (Fig. 5e). In addition, the CLSM images of tumor tissue slides presented enhanced ICG fluorescence at locations that were more distal from the tumor boundary for ARNGs@TMZ/ICG with NIR irradiation than without NIR irradiation (Fig. 5f). Interestingly, the total amounts of TMZ and ICG in brain at 8 h post treatment, combining released and unreleased drugs in the nanogels, were similar between mice treated with ARNGs@TMZ/ICG + L and ARNGs@TMZ/ICG (Fig. 5g, 5h). However, the ICG fluorescence in mice treated with ARNGs@TMZ/ICG boosted upon NIR irradiation (ARNGs@TMZ/ICG + L, Fig. 5c, 5d), implying that the enhanced ICG release from the nanogels as well as the distal tumor drug transfer occurred after the nanogels had been accumulated in tumor site.

Complete suppression of orthotopic U87MG tumors in mice. To evaluate the anti-tumor effect of NIR-activatable ARNGs@TMZ/ICG, we administered various nanogels into orthotopic U87MG-luc bearing

mice via tail vein injection on Day 10, 12, 14, 16, and 18 after the tumor implantations (Fig. 6a). The treatment of orthotopic brain tumor was preliminarily evaluated based on the intensity of tumor bioluminescence. As shown in Fig. 6b, the tumor bioluminescence in the brains of mice treated with ARNGs@TMZ/ICG and NIR irradiation (ARNGs@TMZ/ICG + L) remained almost unchanged, exhibiting supreme tumor suppression by this treatment. As a comparison, the mice receiving monotherapy ARNGs@TMZ or ARNGs@ICG + L displayed less efficient anti-tumor effect, and PBS treatments could hardly restrain tumor proliferation with or without laser irradiation. The quantitative analysis of the bioluminescence intensity further verified the complete inhibition of GBM growth by NIR-activated ARNGs@TMZ/ICG (Fig. 6c), whereas the anti-tumor activity of ARNGs@TMZ/ICG was significantly compromised without NIR activation. Notably, there was no obvious body weight loss for mice treated with NIR-activated ARNGs@TMZ/ICG, demonstrating that the treatment had few side effects to mice (Fig. 6d). In contrast, dramatic body weight reduction was observed for mice treated with PBS, mainly due to the tumor-associated brain dysfunctions. Strikingly, the median survival time of the mice treated with NIR-activated ARNGs@TMZ/ICG was 69 days, which was remarkably longer than those of the mice treated with inactivated ARNGs@TMZ/ICG (43 days), ARNGs@TMZ (34 days), or ARNGs@ICG with NIR irradiation (38 days) (Fig. 6e). The histological analysis of the whole brain using hematoxylin-eosin (H&E) staining showed that NIR-activated ARNGs@TMZ/ICG resulted in minimized tumor size in brain, consistent with the lowest tumor bioluminescence intensity by this treatment (Fig. 6f). Terminal deoxynucleotidyl transferase dUTP nick-end labeling (TUNEL) analysis (Fig. 6g) showed that NIR-activated ARNGs@TMZ/ICG induced the highest levels of apoptosis (caspase 3) and nucleus damage (γH2AX) in tumor cells, and the cell proliferation signal (Ki67) was also the weakest among all the groups (Supplementary Fig. 5). Additionally, NIR-activated ARNGs@TMZ/ICG exhibited negligible side effects to the major normal tissues including heart, liver, spleen, lung, and kidney (Supplementary Fig. 6), demonstrating their good biocompatibility.

Biocompatibility evaluation of ARNGs@TMZ/ICG. We further assessed the biosafety of the NIR-activatable biomimetic nanogels using blood routine and blood biochemistry analysis. ARNGs@TMZ/ICG were intravenously administrated into healthy mice, and the blood was collected and detected on Day 0, 2, 4, 7 and 14 post injection, respectively. ARNGs@TMZ/ICG showed negligible impact on the blood parameters including white blood cell (WBC), red blood cell (RBC), hemoglobin (HGB) and alkaline phosphatase (ALP) (Fig. 7a-d). The blood urea, creatinine (CREA) and carbonic anhydrase (UA) level also exhibit no significant change during the 2 weeks after ARNGs@TMZ/ICG administration (Supplementary Fig. 7). In sharp contrast, the values of alanine aminotransferase (ALT) and aspartate aminotransferase (AST) of the mice treated by mixed solution of TMZ and ICG (Free TMZ/ICG) were significantly higher than those treated by PBS on Day 2 and 4 (Fig. 7e, 7f), implying that the free drugs caused hepatotoxicity. Pro-inflammatory cytokines such as IL-1β, IL-6 and TNF-α were assessed in liver and kidney (Fig. 7g-l), which demonstrated no significant difference between PBS, Free TMZ/ICG, and ARNGs@TMZ/ICG treatment groups after two weeks. However, the Free TMZ/ICG group showed significantly increased pro-inflammatory cytokines on Day 2. Collectively, the biocompatibility evaluation pointed out that

encapsulating TMZ and ICG in our NIR-activatable biomimetic nanogels could effectively reduce the systemic adverse effects of the drugs.

Discussion

To maintain an effective drug concentration in deep tumor lesions remains an unsurmountable challenge in GBM treatment. In the efforts described above, we have developed a NIR-activatable biomimetic nanogel system ARNGs@TMZ/ICG that realizes the deep penetration of TMZ and ICG to distal GBM tumor cells across BBB and other biological barriers. In our design, we highlight the precise activation of ARNGs@TMZ/ICG by ICG-generated ROS upon NIR irradiation. Compared with other ROS-responsive drug delivery systems, the PDDA-based nanogels are inert to endogenous oxidative conditions, which is important to enhance their stability in the circulation system and avoid possible drug leakage in non-tumor microenvironments. The decoration with ApoE-peptide functionalized erythrocyte membrane further extends the circulation time, improves tumor accumulation, and facilitates the BBB penetration of the nanogels. After the nanogels reach effective tumor accumulation, which can be traced by ICG fluorescence, NIR irradiation is manually applied on tumor lesions. ICG then generates ROS to deform the nanogels, triggering burst localized drug release and deep penetration of the drugs to distal tumor cells. Therefore, this activation process is especially favorable to maintain a high concentration of TMZ and ICG in deep GBM lesions. Consequently, the focal synergistic NIR PDT and chemotherapy resulted in complete orthotopic GBM tumor inhibition and significantly improved survival rate, with excellent biocompatibility and minimal side effects. The PDDA-based NIR-activatable nanogels not only offer translational advantages as a potential therapeutic platform against malignant GBM, but also pave a new way to engineer precisely controllable therapies to treat a variety of diseases based on active response towards physiological signals.

Declarations

Acknowledgements

This work was supported by National Natural Science Foundation of China (NSFC 51803049, 21877042, U2004171, 31800841, and 32071388), the National Key Technologies R&D Program of China (2018YFA0209800 and 2018YFA0208903), Program for Science & Technology Innovation Talents in Universities of Henan Province (21HASTIT033).

Author Contributions

Y.Z., B.S. and L.L. designed the experiments, supervised the project, and revised the manuscript. D.Z., S.T. and Y.L. prepared and characterized the nanocapsules and performed in vitro and in vivo experiments. D.Z., S.T. and Y.L. analyzed the data. D.Z. and S.T. wrote the manuscript and revised it with comments from M.Z, Y.Z., B.S. and L.L., all authors participated in discussions throughout the project.

References

1. Tan, A. C.; Ashley, D. M.; López, G. Y.; Malinzak, M.; Friedman, H. S.; Khasraw, M., Management of glioblastoma: State of the art and future directions. *CA Cancer J. Clin.* **2020,** *70* (4), 299-312.

2. Delgado-Martín, B.; Medina, M. Á., Advances in the knowledge of the molecular biology of glioblastoma and its impact in patient diagnosis, stratification, and treatment. *Adv. Sci.* **2020,** *7* (9), 1902971.

3. Tykocki, T.; Eltayeb, M., Ten-year survival in glioblastoma. A systematic review. *J. Clin. Neurosci.* **2018,** *54*, 7-13.

4. Molinaro, A. M.; Hervey-Jumper, S.; Morshed, R. A.; Young, J.; Han, S. J.; Chunduru, P.; Zhang, Y.; Phillips, J. J.; Shai, A.; Lafontaine, M.; Crane, J.; Chandra, A.; Flanigan, P.; Jahangiri, A.; Cioffi, G.; Ostrom, Q.; Anderson, J. E.; Badve, C.; Barnholtz-Sloan, J.; Sloan, A. E.; Erickson, B. J.; Decker, P. A.; Kosel, M. L.; LaChance, D.; Eckel-Passow, J.; Jenkins, R.; Villanueva-Meyer, J.; Rice, T.; Wrensch, M.; Wiencke, J. K.; Oberheim Bush, N. A.; Taylor, J.; Butowski, N.; Prados, M.; Clarke, J.; Chang, S.; Chang, E.; Aghi, M.; Theodosopoulos, P.; McDermott, M.; Berger, M. S., Association of maximal extent of resection of contrast-enhanced and non–contrast-enhanced tumor with survival within molecular subgroups of patients with newly diagnosed glioblastoma. *JAMA Oncol.* **2020,** *6* (4), 495-503.

5. Lara-Velazquez, M.; Al-Kharboosh, R.; Jeanneret, S.; Vazquez-Ramos, C.; Mahato, D.; Tavanaiepour, D.; Rahmathulla, G.; Quinones-Hinojosa, A., Advances in brain tumor surgery for glioblastoma in adults. *Brain Sci.* **2017,** *7* (12), 166-182.

6. Hochberg, F. H.; Pruitt, A., Assumptions in the radiotherapy of glioblastoma. *Neurology* **1980,** *30* (9), 907.

7. Parney, I. F.; Chang, S. M., Current Chemotherapy for Glioblastoma. *The Cancer Journal* **2003,** *9* (3).

8. Cramer, S. W.; Chen, C. C., Photodynamic Therapy for the Treatment of Glioblastoma. **2020,** *6* (81).

9. Shergalis, A.; Bankhead, A.; Luesakul, U.; Muangsin, N.; Neamati, N., Current challenges and opportunities in treating glioblastoma. *Pharmacol. Rev.* **2018,** *70* (3), 412-445.

10. Ghosh, D.; Nandi, S.; Bhattacharjee, S., Combination therapy to checkmate Glioblastoma: clinical challenges and advances. *Clin. Trans. Med.* **2018,** *7* (1), 33-45.

11. Cha, G. D.; Kang, T.; Baik, S.; Kim, D.; Choi, S. H.; Hyeon, T.; Kim, D.-H., Advances in drug delivery technology for the treatment of glioblastoma multiforme. *J. Control. Release* **2020,** *328*, 350-367.

12. Chauhan, V. P.; Jain, R. K., Strategies for advancing cancer nanomedicine. *Nat. Mater.* **2013,** *12* (11), 958-962.

13. Jain, R. K.; Stylianopoulos, T., Delivering nanomedicine to solid tumors. *Nat. Rev. Clin. Oncol.* **2010,** *7* (11), 653-664.

14. Mitchell, M. J.; Billingsley, M. M.; Haley, R. M.; Wechsler, M. E.; Peppas, N. A.; Langer, R., Engineering precision nanoparticles for drug delivery. *Nat. Rev. Drug Discov.* **2021,** *20* (2), 101-124.

15. Fan, W.; Yung, B.; Huang, P.; Chen, X., Nanotechnology for Multimodal Synergistic Cancer Therapy. *Chem. Rev.* **2017,** *117* (22), 13566-13638.

16. Ganipineni, L. P.; Danhier, F.; Préat, V., Drug delivery challenges and future of chemotherapeutic nanomedicine for glioblastoma treatment. *J. Control. Release* **2018,** *281*, 42-57.

17. Jiang, Y.; Zhang, J.; Meng, F.; Zhong, Z., Apolipoprotein E peptide-directed chimeric polymersomes mediate an ultrahigh-efficiency targeted protein therapy for glioblastoma. *ACS Nano* **2018,** *12* (11), 11070-11079.

18. Hartl, N.; Adams, F.; Merkel, O. M., From adsorption to covalent bonding: Apolipoprotein E functionalization of polymeric nanoparticles for drug delivery across the blood–brain barrier. *Adv. Therap.* **2021,** *4* (1), 2000092.

19. Ruan, H.; Hu, Q.; Wen, D.; Chen, Q.; Chen, G.; Lu, Y.; Wang, J.; Cheng, H.; Lu, W.; Gu, Z., A Dual-Bioresponsive Drug-Delivery Depot for Combination of Epigenetic Modulation and Immune Checkpoint Blockade. *Adv. Mater.* **2019,** *31* (17), 1806957.

20. Huang, S.; Shao, K.; Liu, Y.; Kuang, Y.; Li, J.; An, S.; Guo, Y.; Ma, H.; Jiang, C., Tumor-Targeting and Microenvironment-Responsive Smart Nanoparticles for Combination Therapy of Antiangiogenesis and Apoptosis. *ACS Nano* **2013,** *7* (3), 2860-2871.

21. Ju, E.; Dong, K.; Liu, Z.; Pu, F.; Ren, J.; Qu, X., Tumor Microenvironment Activated Photothermal Strategy for Precisely Controlled Ablation of Solid Tumors upon NIR Irradiation. *Adv. Funct. Mater.* **2015,** *25* (10), 1574-1580.

22. Zhou, Q.; Shao, S.; Wang, J.; Xu, C.; Xiang, J.; Piao, Y.; Zhou, Z.; Yu, Q.; Tang, J.; Liu, X.; Gan, Z.; Mo, R.; Gu, Z.; Shen, Y., Enzyme-activatable polymer–drug conjugate augments tumour penetration and treatment efficacy. *Nat. Nanotech.* **2019,** *14* (8), 799-809.

23. Li, J.; Yu, X.; Wang, Y.; Yuan, Y.; Xiao, H.; Cheng, D.; Shuai, X., A Reduction and pH Dual-Sensitive Polymeric Vector for Long-Circulating and Tumor-Targeted siRNA Delivery. *Adv. Mater.* **2014,** *26* (48), 8217-8224.

24. Li, H.-J.; Du, J.-Z.; Liu, J.; Du, X.-J.; Shen, S.; Zhu, Y.-H.; Wang, X.; Ye, X.; Nie, S.; Wang, J., Smart Superstructures with Ultrahigh pH-Sensitivity for Targeting Acidic Tumor Microenvironment: Instantaneous Size Switching and Improved Tumor Penetration. *ACS Nano* **2016,** *10* (7), 6753-6761.

25. Chauhan, V. P.; Stylianopoulos, T.; Boucher, Y.; Jain, R. K., Delivery of Molecular and Nanoscale Medicine to Tumors: Transport Barriers and Strategies. *Ann. Rev. Chem. Biomol. Eng.* **2011,** *2* (1), 281-298.

26. Greten, F. R.; Grivennikov, S. I., Inflammation and Cancer: Triggers, Mechanisms, and Consequences. *Immunity* **2019,** *51* (1), 27-41.

27. Mantovani, A., The inflammation – cancer connection. *The FEBS Journal* **2018,** *285* (4), 638-640.

28. Saravanakumar, G.; Kim, J.; Kim, W. J., Reactive-oxygen-species-responsive drug delivery systems: promises and challenges. *Adv. Sci.* **2017,** *4* (1), 1600124.

29. Kwon, S.; Ko, H.; You, D. G.; Kataoka, K.; Park, J. H., Nanomedicines for reactive oxygen species mediated approach: An emerging paradigm for cancer treatment. *Acc. Chem. Res.* **2019,** *52* (7), 1771-1782.

30. Xu, X.; Saw, P. E.; Tao, W.; Li, Y.; Ji, X.; Bhasin, S.; Liu, Y.; Ayyash, D.; Rasmussen, J.; Huo, M.; Shi, J.; Farokhzad, O. C., ROS-responsive polyprodrug nanoparticles for triggered drug delivery and effective cancer therapy. *Adv. Mater.* **2017,** *29* (33), 1700141.

31. Ballance, W. C.; Qin, E. C.; Chung, H. J.; Gillette, M. U.; Kong, H., Reactive oxygen species-responsive drug delivery systems for the treatment of neurodegenerative diseases. *Biomaterials* **2019,** *217*, 119292.

32. Popa-Wagner, A.; Mitran, S.; Sivanesan, S.; Chang, E.; Buga, A.-M., ROS and Brain Diseases: The Good, the Bad, and the Ugly. *Oxid. Med. and Cell. Longev.* **2013,** *2013*, 963520.

33. Dumont, M.; Beal, M. F., Neuroprotective strategies involving ROS in Alzheimer disease. *Free Radic. Biol. Med.* **2011,** *51* (5), 1014-1026.

34. Ahmad, W.; Ijaz, B.; Shabbiri, K.; Ahmed, F.; Rehman, S., Oxidative toxicity in diabetes and Alzheimer's disease: mechanisms behind ROS/ RNS generation. *J. Biomed. Sci.* **2017,** *24* (1), 76.

35. Tian, S.; Li, H.; Li, Z.; Tang, H.; Yin, M.; Chen, Y.; Wang, S.; Gao, Y.; Yang, X.; Meng, F.; Lauher, J. W.; Wang, P.; Luo, L., Polydiacetylene-based ultrastrong bioorthogonal Raman probes for targeted live-cell Raman imaging. *Nat. Commun.* **2020,** *11* (1), 81.

36. Tian, S.; Yue, Q.; Liu, C.; Li, M.; Yin, M.; Gao, Y.; Meng, F.; Tang, B. Z.; Luo, L., Complete degradation of a conjugated polymer into green upcycling products by sunlight in air. *J. Am. Chem. Soc.* **2021,** *143* (27), 10054-10058.

37. Wang, H.; Wang, X.; Xie, C.; Zhang, M.; Ruan, H.; Wang, S.; Jiang, K.; Wang, F.; Zhan, C.; Lu, W.; Wang, H., Nanodisk-based glioma-targeted drug delivery enabled by a stable glycopeptide. *J. Control. Release* **2018,** *284*, 26-38.

38. Mantle, J. L.; Min, L.; Lee, K. H., Minimum transendothelial electrical resistance thresholds for the study of small and large molecule drug transport in a human in vitro blood–brain barrier model. *Mol. Pharmaceut.* **2016,** *13* (12), 4191-4198.

39. Wei, J.; Xia, Y.; Meng, F.; Ni, D.; Qiu, X.; Zhong, Z., Small, smart, and LDLR-specific micelles augment sorafenib therapy of gioblastoma. *Biomacromolecules* **2021,** *22*, 4814-4822.

40. Pucci, C.; Marino, A.; Şen, Ö.; De Pasquale, D.; Bartolucci, M.; Iturrioz-Rodríguez, N.; di Leo, N.; de Vito, G.; Debellis, D.; Petretto, A.; Ciofani, G., Ultrasound-responsive nutlin-loaded nanoparticles for combined chemotherapy and piezoelectric treatment of glioblastoma cells. *Acta Biomater.* **2021**, DOI: 10.1016/j.actbio.2021.04.005.

41. Li, B.; Zhao, M.; Feng, L.; Dou, C.; Ding, S.; Zhou, G.; Lu, L.; Zhang, H.; Chen, F.; Li, X.; Li, G.; Zhao, S.; Jiang, C.; Wang, Y.; Zhao, D.; Cheng, Y.; Zhang, F., Organic NIR-II molecule with long blood half-life for in vivo dynamic vascular imaging. *Nat. Commun.* **2020,** *11* (1), 3102.

42. Zorzi, A.; Middendorp, S. J.; Wilbs, J.; Deyle, K.; Heinis, C., Acylated heptapeptide binds albumin with high affinity and application as tag furnishes long-acting peptides. *Nat. Commun.* **2017,** *8* (1), 16092.

Figures

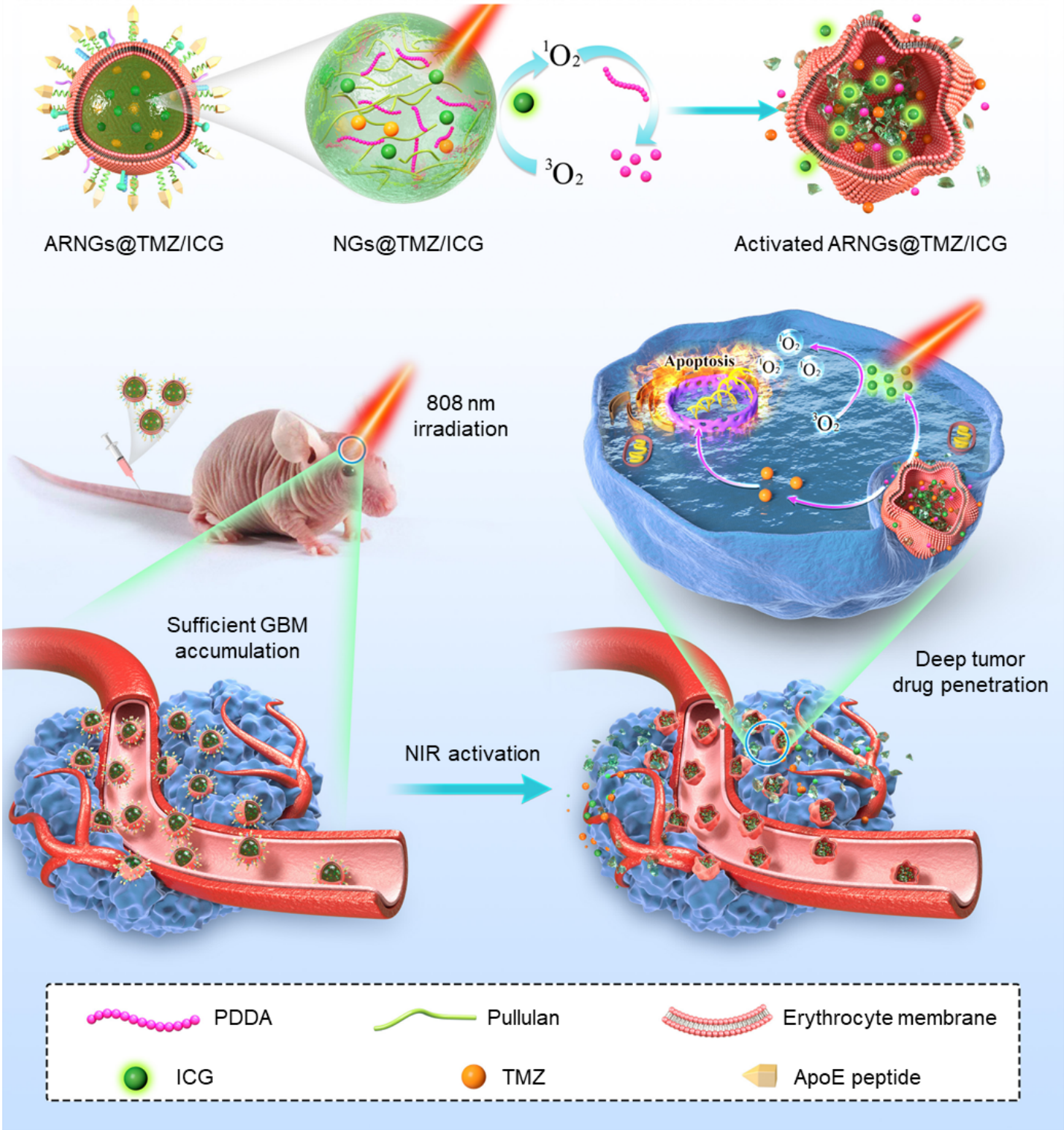

Figure 1

Schematic illustration of NIR-activatable biomimetic nanogels ARNGs@TMZ/ICG enabling deep tumor penetration and accumulation of TMZ and ICG for orthotopic GBM treatment.

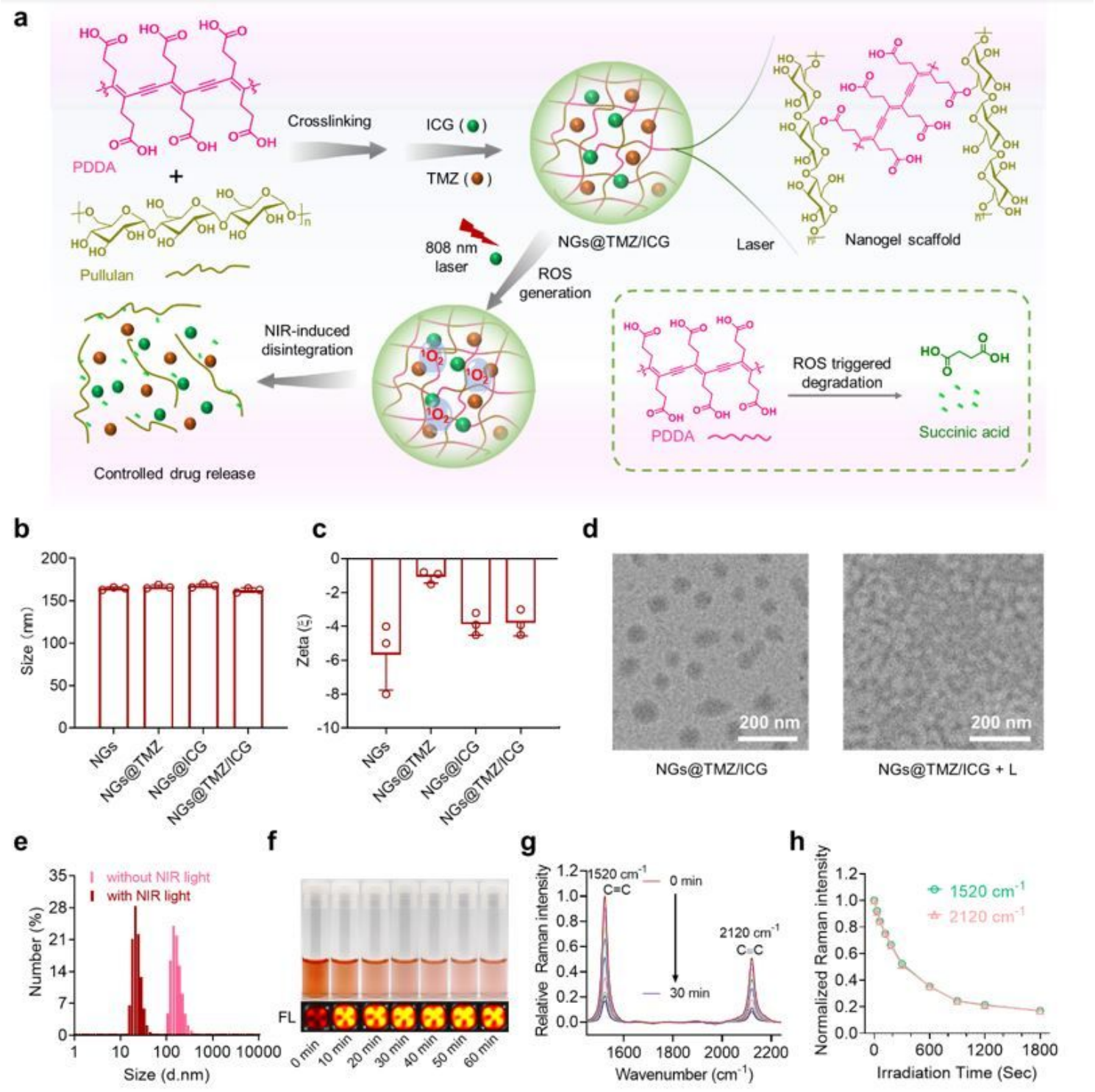

Figure 2

Preparation and NIR-induced disintegration of NGs@TMZ/ICG. a, Schematic illustration of the synthesis of the nanogels and their NIR-induced disintegration. **b**, **c**, Size distribution (**b**) and zeta potential (**c**) of the corresponding nanoparticles measured by DLS. **d**, TEM images of the NGs@TMZ/ICG before and after NIR irradiation (808 nm, 0.5 W cm^{-2}, 5 min). **e**, Particle sizes of NGs@TMZ/ICG before and after NIR irradiation (808 nm, 0.5 W cm^{-2}, 5 min) measured by DLS. **f**, Photographs and the florescence images (FL)

of the RB-containing nanogels upon light irradiation for different time (520 nm, 5 mW cm^{-2}). **g**, Raman spectra of NGs@TMZ/ICG after exposure to NIR irradiation for different time (808 nm, 0.5 W cm^{-2}). **h**, Change in the normalized Raman intensity of C=C bonds (1520 cm^{-1}) and C≡C bonds (2120 cm^{-1}) as a function of sunlight irradiation time.

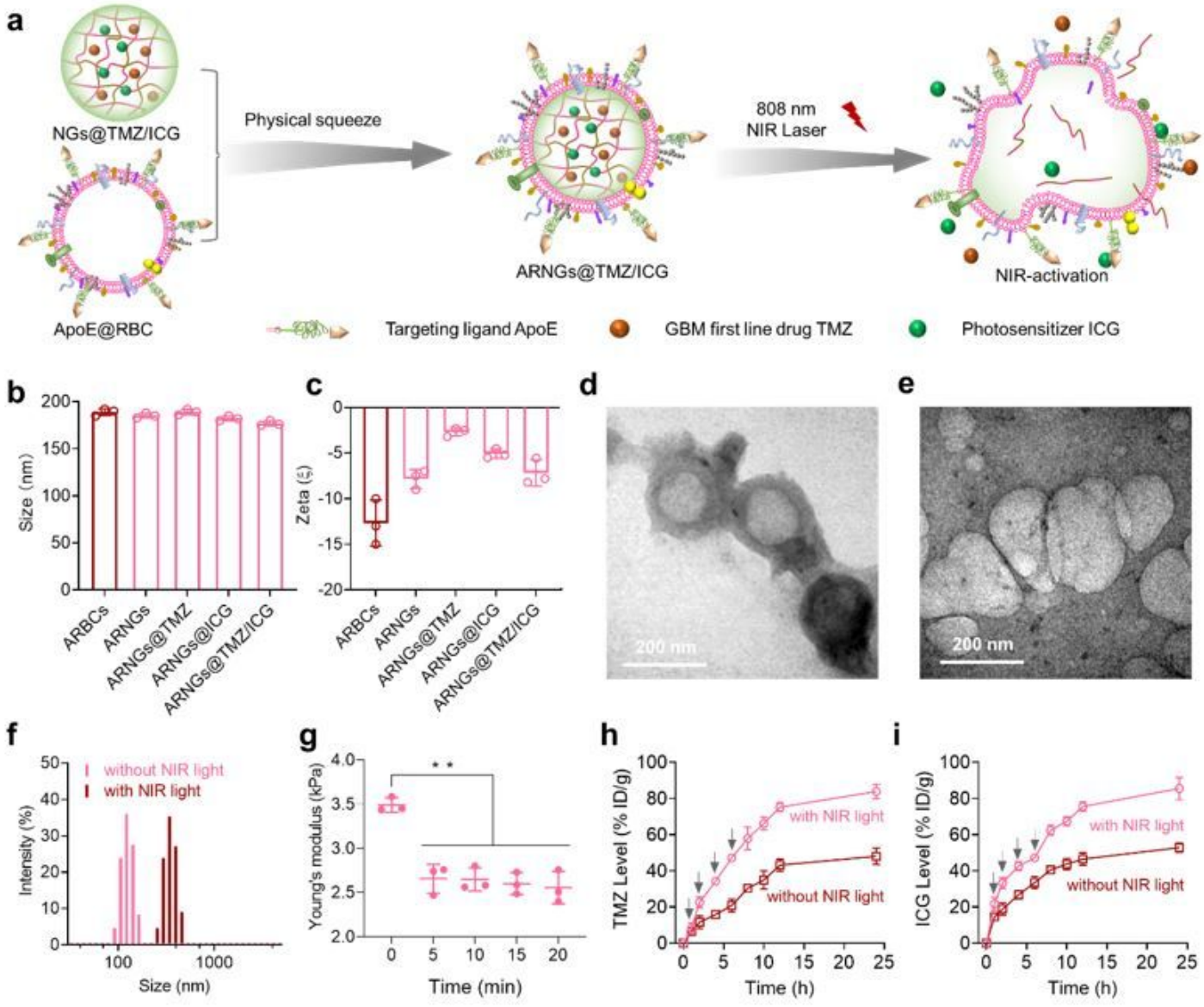

Figure 3

Preparation of ARNGs@TMZ/ICG and NIR-induced deformation. a, Schematic illustration of camouflaging ARNGs@TMZ/ICG by ApoE peptide-decorated erythrocyte membranes and NIR-induced deformation of the nanogels. **b**, **c**, Size distribution (**b**) and zeta potential **(c)** of various nanoparticles measured by DLS. **d**, **e**, TEM images of ARNGs@TMZ/ICG before (**d**) and after (**e**) NIR irradiation (808 nm, 0.5 W cm^{-2}, 5 min). **f**, Particle size distribution of ARNGs@TMZ/ICG with and without NIR irradiation (808 nm, 0.5 W cm^{-2}, 5 min). **g**, Young's modulus of ARNGs@TMZ/ICG after receiving different time of NIR

irradiation (808 nm, 0.5 W cm^{-2}) measured by AFM (n = 3). **h**, **i**, In vitro release profile of TMZ (**h**) and ICG (**i**) from ARNGs@TMZ/ICG in pH 7.4 phosphate buffer at 37 °C, with and without NIR irradiation (808 nm, 0.5 W cm^{-2}). Data are presented as mean ± SD (one-way ANOVA and Tukey's multiple comparison test; $^{**}p<0.01$).

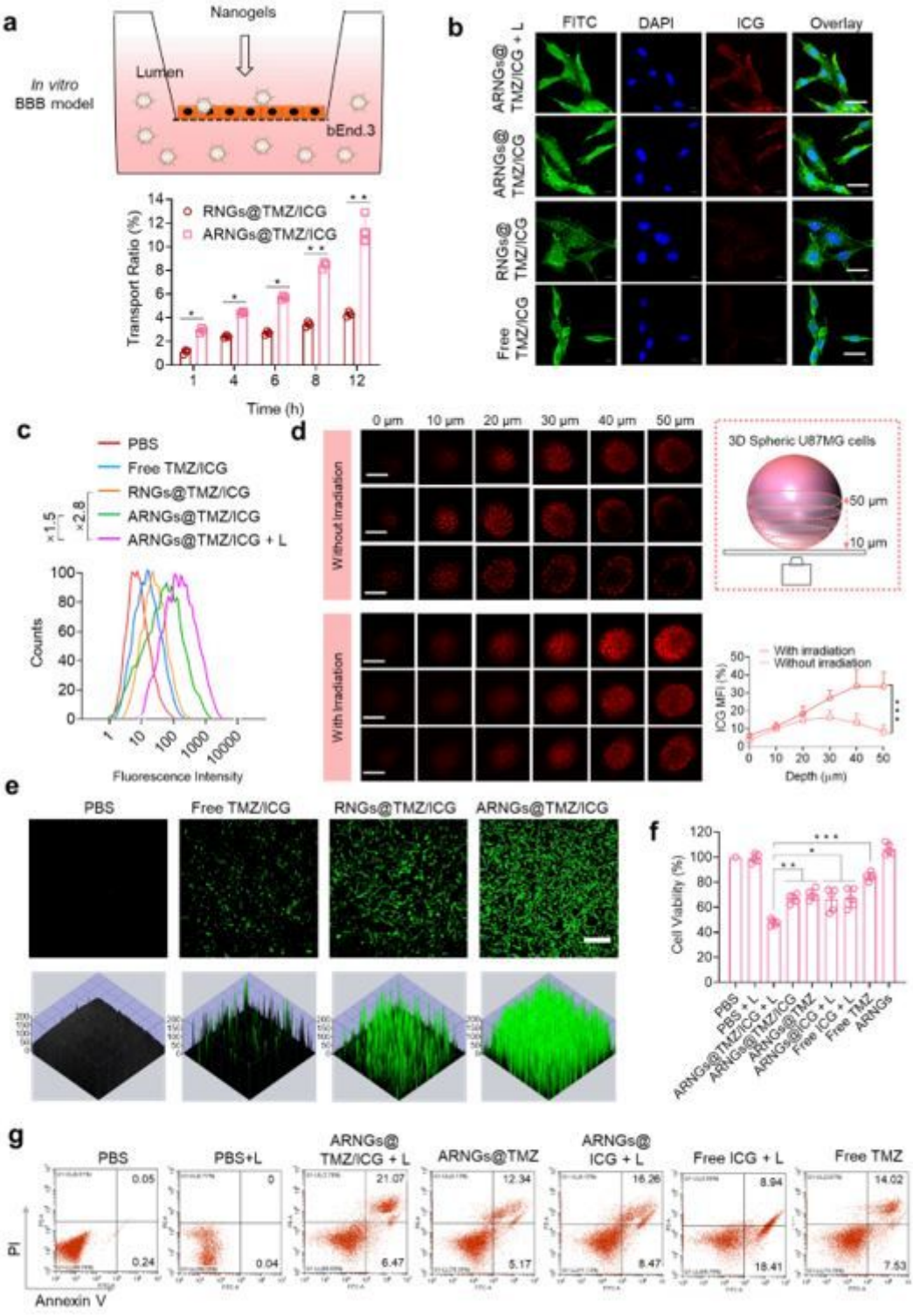

Figure 4

In vitro BBB penetration, cellular and tumor uptake, and cytotoxicity of biomimetic nanogels. a, Cumulative transport ratio of ARNGs@ICG and RNGs@ICG across of the *in vitro* BBB trans-well model at different time (n = 3). **b**, CLSM images of U87MG cells receiving various treatments and stained by fluorescein 5-isothiocyanate (FITC) and 4',6-diamidino-2-phenylindole dihydrochloride (DAPI). Scale bar: 20 μm. **c**, Flow cytometry analysis of U87MG cells receiving various treatments. **d**, Uptake of ARNGs@TMZ/ICG by U87MG multicellular spheroids after 4 h of incubation with and without NIR irradiation. Z-stack imaging was progressed from the bottom into the core of the spheroids at an interval of 10 μm. Scale bar: 200 μm; Top right: Schematic diagram of the 3D spherical U87MG model; Bottom right: Quantification of the relative ICG mean fluorescence intensity (MFI, n = 3). **e**, CLSM images of DCFH-DA-stained U87MG cells after incubating with various nanogels for 4 h upon NIR irradiation. Scale bar: 100 μm. **f**, Cell viability of U87MG cells by MTT assay at 24 h after receiving various treatments (n = 5). **g**, Apoptosis analysis of U87MG cells by flow cytometry at 18 h after receiving various treatments and stained by PI and Annexin V. For all studies, incubation time with treatment agents: 4 h; NIR: 808 nm, 0.5 W cm^{-2}, 5 min; ICG conc0 entration: 10 μg mL^{-1}; TMZ concentration: 10 μg mL^{-1}; Data are presented as mean ± SD (one-way ANOVA and Tukey's multiple comparison test; *p<0.05, **p<0.01, ***p<0.001).

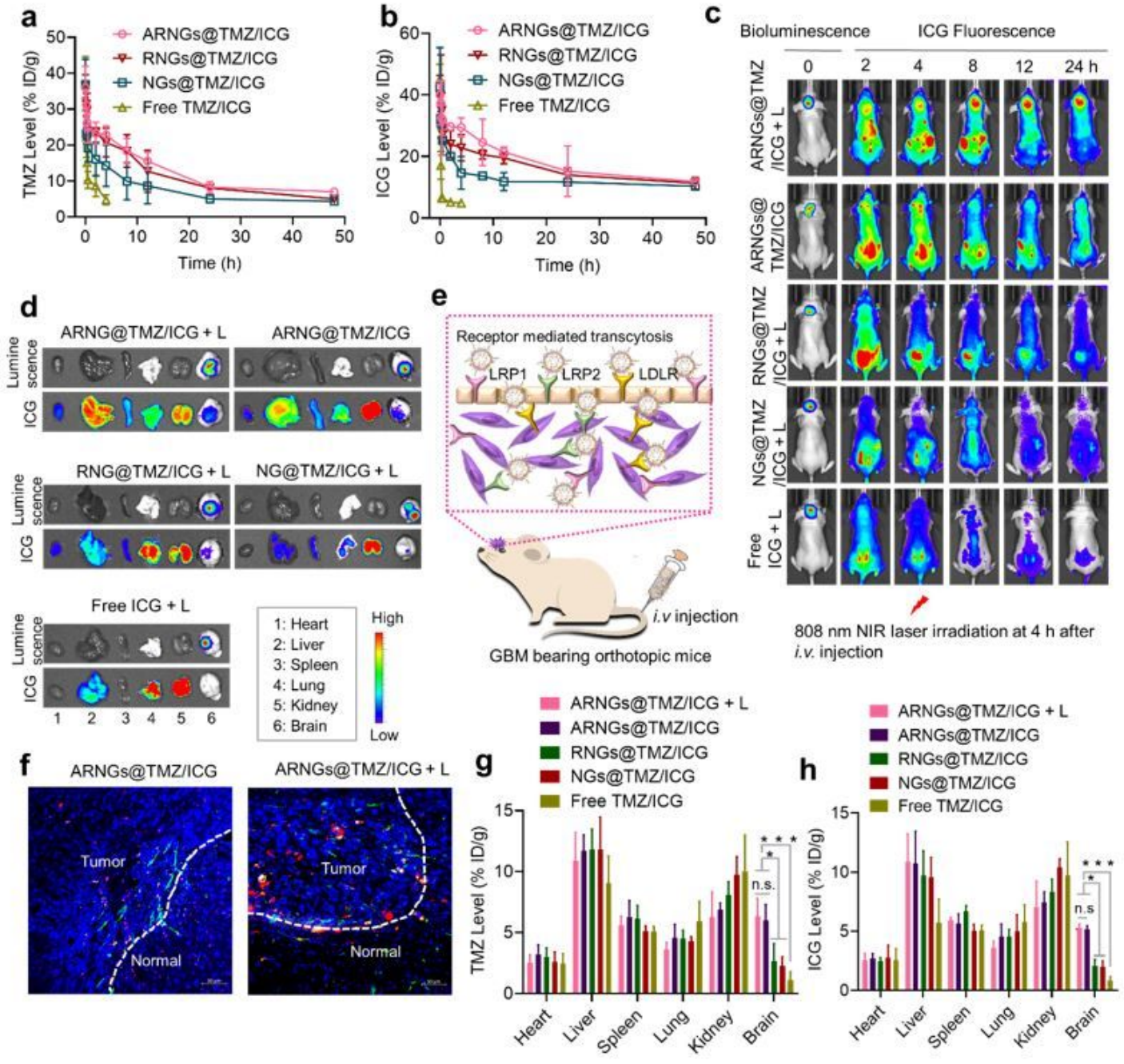

Figure 5

Pharmacokinetics, in vivo BBB penetration, and biodistribution of NIR-activatable ARNGs@TMZ/ICG. a, **b**, Pharmacokinetics of TMZ **(a)** and ICG **(b)** from ARNGs@TMZ/ICG in healthy BALB/c mice, TMZ and ICG levels were determined by HPLC and fluorescence spectroscopy, respectively, and expressed as injected dose per gram (%ID g^{-1}). **c**, The IVIS images of the tumor-bearing mice taken at different time after receiving various treatments. **d**, ICG fluorescence images of the major organs (heart, liver, spleen, lung, kidney and brain) taken from the tumor bearing mice at 8 h after receiving various treatments shown in **c**. **e**, Schematic illustration of the uptake of ARNGs@TMZ/ICG by specifically targeting to LDL receptors overexpressed on both BBB endothelial cells and brain tumor cells. **f**, Fluorescence images of tumor

tissue slides from the mice treated with ARNGs@TMZ/ICG and ARNGs@TMZ/ICG + L. The tumor slices were taken from the mice at 8 h post injection. The green fluorescence referred to CD31-labeled tumor blood vessels. **g**, **h**, Quantification of TMZ **(g)** and ICG **(h)** accumulation in different organs from the tumor bearing mice at 8 h after receiving different treatments. In studies of Fig. 3c-3h, orthotopic U87MG-Luc tumor bearing mice were used, and all agents were intravenously administered. The dosage was 10 mg kg^{-1} for both TMZ and ICG. NIR irradiation (808 nm, 1 W cm^{-2}, 5 min) was applied at 4 h post injection. Data are presented as mean ± SD (one-way ANOVA and Tukey multiple comparisons tests, *p < 0.05, **p < 0.01, ***p < 0.001, n.s. represents no significance).

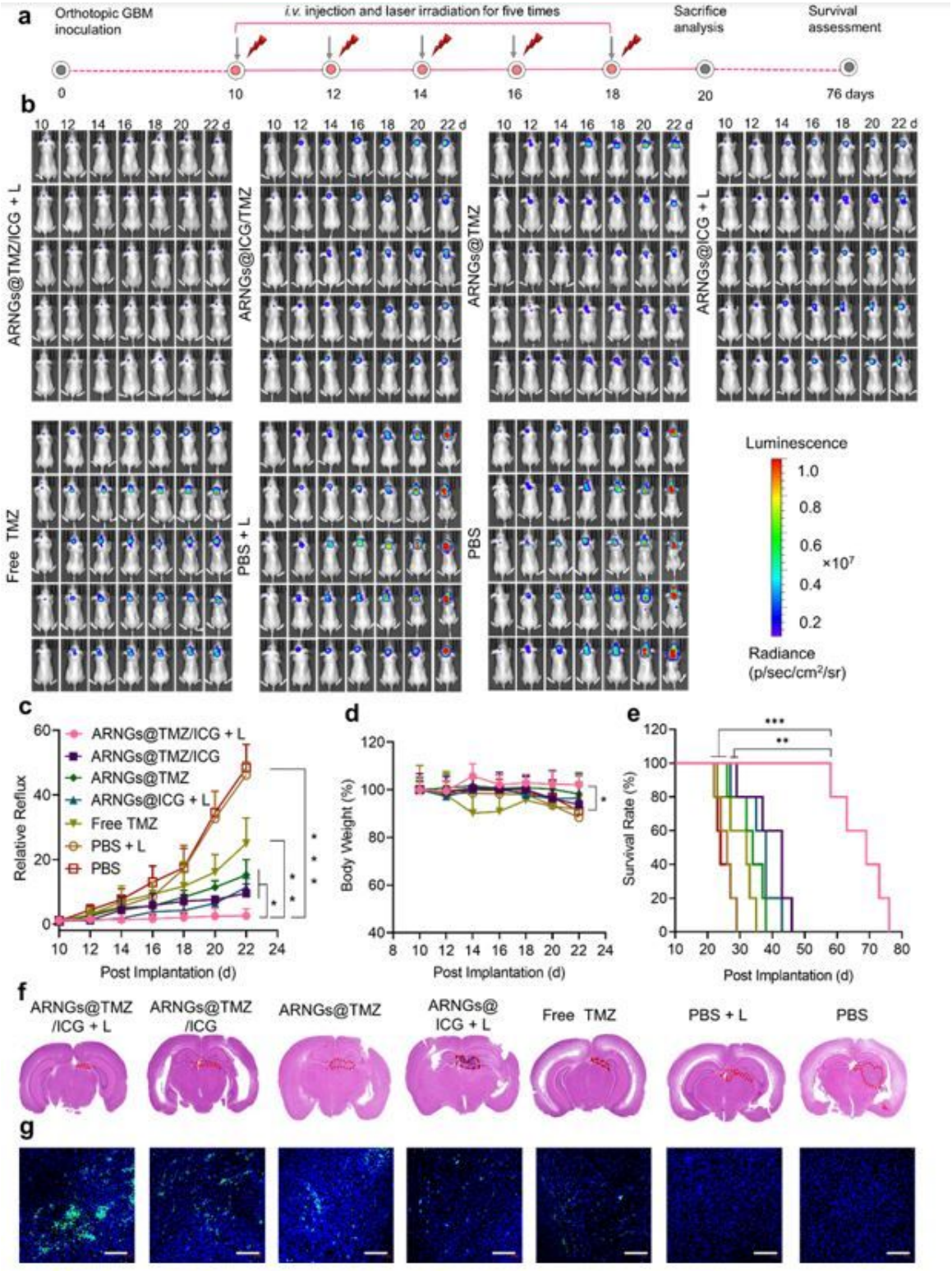

Figure 6

Anti-tumor efficacy of NIR-activatable ARNGs@TMZ/ICG against orthotopic GBM. a, Schematic illustration of the timeline of the anti-tumor efficacy studies on orthotopic GBM bearing mice. U87MG-Luc cells were orthotopically inoculated into the brains of 6-8 weeks nude mice. On Day 10 after the tumor inoculation, mice with a similar bioluminescence intensity were selected and randomized into 7 groups (n = 5). Various formulations were intravenously injected at a dose of 10 mg TMZ equiv. kg^{-1} and 10 mg ICG

equiv. kg^{-1} on Day 10, 12, 14, 16, and 18 post tumor implantation. **b**, *In vivo* bioluminescence images of orthotopic GBM in live mice receiving different treatments. **c**, Quantified tumor bioluminescence levels of orthotopic GBM in each group. **d**, Body-weight changes in mice. **e**, Kaplan-Meier analysis of the mice. **f**, H&E-staining images of the orthotopic brain tumor tissues excised from the mice in each group. **g**, TUNEL-staining images of the orthotopic brain tumor tissues excised from the mice in each group. Scale bars: 100 μm. Data are presented as mean ± SD (one-way ANOVA and Tukey multiple comparisons tests, $*p < 0.05$, $**p < 0.01$, $***p < 0.001$).

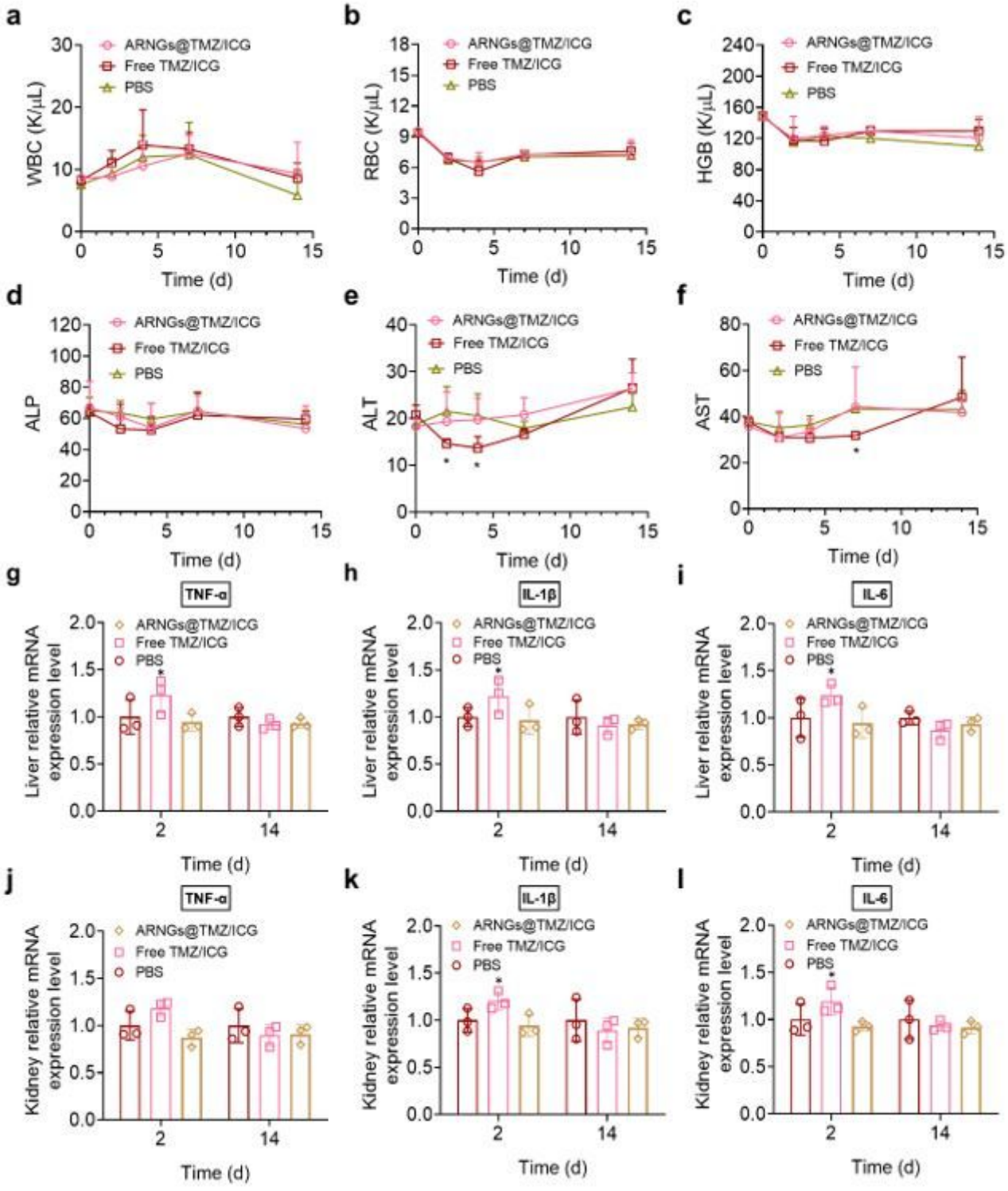

Figure 7

Biocompatibility evaluation of NIR-activatable ARNGs@TMZ/ICG. a-c, Cytotoxicity and in vivo biocompatibility assessment of ARNGs@TMZ/ICG. (**a**) White blood cell (WBC), (**b**) red blood cell (RBC) and (**c**) hemoglobin (HGB) levels in blood samples were assessed after a single dose tail vein injection. **d-f**, Blood chemistry examinations. Plasma (**d**) alkaline phosphatase (ALP), (**e**) alanine aminotransferase (ALT) and (**f**) aspartate aminotransferase (AST) levels after a single dose tail vein injection. **g-l**, Expression of sentinel proinflammatory cytokines TNF-α, Il-1β and Il-6 in liver **(g-i)** and kidney **(j-l)** assessed on Day 2 and 14 after a single dose tail vein injection. Data are presented as mean ± SD (n = 4, one-way ANOVA and Tukey multiple comparisons tests, *p < 0.05).

Supplementary Files

This is a list of supplementary files associated with this preprint. Click to download.

- SupplementaryMaterial.docx